Supplemental Material

Metalens-integrated compact imaging devices for wide-field microscopy

Beibei Xu,[a,c,†] Hanmeng Li,[a,c,†] Shenglun Gao,[a,c] Xia Hua,[b] Cheng Yang,[b] Chen Chen,[a,c] Feng Yan,[b] Shining Zhu,[a,c] and Tao Li[a,c,*]

[a] Nanjing University, National Laboratory of Solid State Microstructures, Key Laboratory of Intelligent Optical Sensing and Integration, Jiangsu Key Laboratory of Artificial Functional Materials, College of Engineering and Applied Sciences, Nanjing, China, 210093

[b] School of Electronic Science and Engineering, Nanjing University, Nanjing, China, 210093

[c] Collaborative Innovation Center of Advanced Microstructures, Nanjing, China, 210093

Section S1: Experimental Methods

Sample preparation: An 850-nm-thick α-Si film was deposited on a 200-μm-thick fused silica substrate by plasma-enhanced chemical vapor deposition (PECVD) with a 5% mixture of silane in argon at 300 °C. Positive electron beam resist (150 nm, PMMA) was then spin-coated. The metalens pattern was defined in the resist using electron beam lithography (EBL, ELS-F125, Elionix). After developing the resist, the pattern was transferred into a 30-nm thick chromium layer deposited by electron beam evaporation (EBE) using the lift-off technique. The patterned chromium served as hard mask for the dry etching of the 850-nm thick α-silicon layer in a mixture of C_4F_8 and SF_6 plasma (HSE200, Sevenstar). Finally, the chromium mask was removed using a solution of ammonium cerium nitrate.

Metalens integration: The optical clear adhesive (OCA) tape (Tesa, 69402) is a double-side tape with sandwiched structure and the intermediate adhesive has well-defined thickness, such as 50 μm, 100 μm, 200 μm and so on (50 μm in our experiments). The whole piece of optical clear adhesive (OCA) tape (Tesa, 69402) is split into small pieces of appropriate size with cutting knife. The 50 μm PET release liner can be easily peeled off with tweezers. Stick the OCA tape onto the

1

encapsulation glass of CMOS image sensor, then peel off the release liner on the other side, and leave the intermedium adhesive on CMOS image sensor. Finally, the metalens or metalens array is fixed with the OCA on sensor.

Optical measurenments: A broadband halogen lamp with band-pass filters at bandwidth of 10 nm (Thorlabs, FB-10 series) is employed as the illumination source. Quarter-wave plates (QWP, Thorlabs, AHWP05M-600) and linear polarizers (LP, Thorlabs, WP25M-VIS) are added to properly select the incident circular polarization state. The MIID is mounted on translation stage (Thorlabs, MBT616D/M), which can be carefully adjusted along the optical direction.
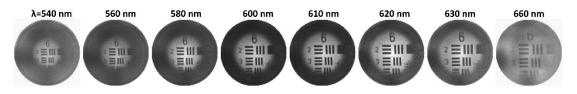
Section S2: Differences between measured and theoretical resolution

Generally speaking, the larger NA of lens means larger diffraction angle and lower diffraction efficiency, which causes larger discrepancy between measured and expected resolution. The resolution discrepancy for NA=0.12 is about 0.71 (here we calculate the discrepancy as r_Δ/r_t, where $r_\Delta=|r_t-r_m|$, r_t and r_m represent the theoretical and measured resolution respectively) while the resolution discrepancy is about 1.38 for NA=0.37.

Section S3: Spectral zooming of MIID

Wavelength range of MIID : There are two main limitations in imaging function of MIID at different wavelengths in practical applications. (1) The efficiency and SNR of both metalens and CMOS sensor. As we taken Si as our metalens material, the wavelength range is reduced to long wavelength in visible due to the absorption loss in blue and green region. The wavelength range can be widened by using transparent material in visible like Silicon nitride. On the other hand, the quantum efficiency of the CMOS sensor is lower at longer wavelength range (<20% at wavelength>700 nm), this will introduced fluctuations and noises. (2) Image magnification. As we mentioned in the manuscript, magnified image suffered from low SNR. Moreover, the operating wavelength also limited by the constricted object space, which depends on the focal length and effect the image magnification. To sum up, the wavelength range is various for different MIID

design, and taken the design in our manuscript into consideration, the wavelength range that shows acceptable performance is about 540 nm~660 nm as shown below.

Fig. S1 The image of 1951 USAF resolution test chart (group 6) taken from MIID at wavelength of 560 nm, 580 nm, 600 nm, 610 nm, 620 nm and 630 nm.

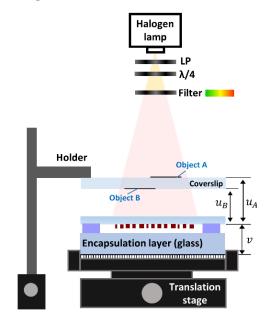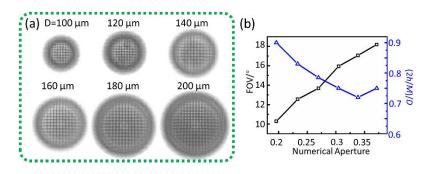## Optical setup for spectral zooming of MIID

Fig. S2 Schematic diagrams of optical setup for spectral zooming of MIID. Once the image of object B at underneath side of coverslip is obtained at object distance u_B with wavelength λ_B, the image of other object at different depth, such as object A at top side of coverslip, is obtained at object distance u_A with wavelength λ_A by tuning the operating wavelength with different filters.
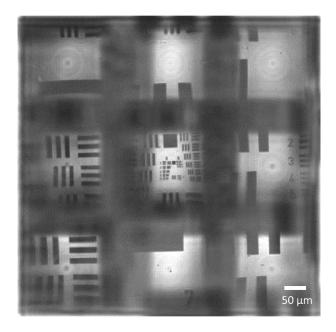
Section S4: Field-of-view (FOV) characterization of metalens

The FOV of metalens with different NAs were characterized with filters of 10 nm bandwidth. The metalenses have same focal length (250 μm) and different diameters from 100 μm to 200 μm with step of 20 μm (Figure S3(a)). Here we define angle of FOV as $2\tan^{-1}(h/v)$, where h is half size of the image that can be clearly distinguished, and v is the imaging distance. The angle of FOV at different NAs is plotted in Fig. S3(b), which increases with increased NA owing to the increased

size of metalens. The largest angle of FOV is about 18°, which is much smaller than a standard lens. In this situation, monochromatic aberrations such as coma and astigmatism do not influence the image quality remarkably yet. Meanwhile, we define $(2h/M)/D$ (here M is the image magnification) as the image ratio, which reflects the relative size of imaging object with respect to metalens. The image ratio reduces firstly and slightly increases afterwards with the increase of NA. We believe that this trend is caused by the lower efficiency of incident light at large angle for higher NA. The image ratio <1 results in image blind area when we arrange metalens in array.

Fig. S3 (a) Images for FOV characterization of metalens with different NAs. The metalenses have same focal length and different diameters from 100 μm to 200 μm with step of 20 μm. (b) The angle of FOV and image height ratio obtained from (a).
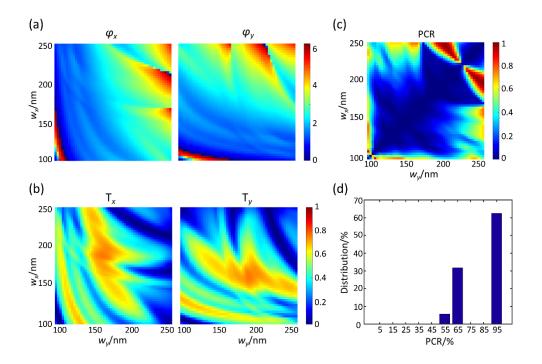
Although the lens array with metalens of square geometry appears to cover the entire image plane, the limited FOV, lower efficiency at corners of metalens and distorted image will result in incomplete image. Moreover, the technique of image stitching needs a certain overlap among sub-images. Fig. S4 shows image of resolution test chart taken from MIID with a 3×3 metalens array at 4f imaging scheme. Each metalens with square geometry here has a size of 200 μm and focal length of 250 μm. The operating wavelength is 630 nm. Obviously, parts of the whole image are missing due to the limited FOV area, such as the symbol "6" for Group 6.

Fig. S4 Images of 1951 USAF resolution test chart taken from MIID with a 3×3 square metalens array at 4f imaging scheme.

Section S5: Design of polarization-multiplexed dual-phase (PMDP) metalens.
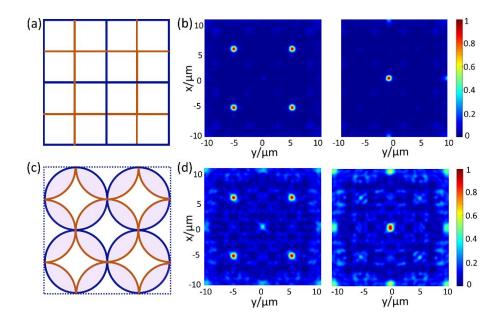
In order to make up the blind area among limited FOV of metalens without mechanical moving, we can utilize the polarization-multiplexed two sets of metalens array to cover whole area, as has indicated in Fig. 4(a). The specific design method of PMDP metalens is as described in ref. [24]. Here, we choose rectangular α-Si nano-posts with height 800 nm and widths w_x and w_y as nanostructure. The simulations were performed with finite-difference time-domain (FDTD) method by using a commercial FDTD software (Lumerical). The x- and y-polarization plane wave were illuminated from substrate to the nano-post arranged in square lattice. A library that determines the relation between the phase shifts (φ_x, φ_y) and the dimensions of the nanostructures are established by parameter sweep at the designed wavelength. The widths w_x and w_y ranged from 100 nm to 250 nm with lattice constant of 400 nm. Fig. S5(a) and S5(b) show the simulated phase shifts and intensity of the transmission coefficients respectively.

5

We also simulated the polarization conversion rate (PCR) for each nanostructure as shown in Fig. S5(c). We counted the PCR distribution of nanostructures for a PMDP metalens with diameter of 200 μm as shown in Fig. S5(d). The average PCR is about 84.09% for left-hand circular polarization (LCP) to right-hand circular polarization (RCP) at wavelength of 630 nm, which is a little bit lower than the former normal metalens with PCR=97.78% at wavelength of 630 nm with w_x =200 nm and w_y =80 nm due to the multiplexing design.

Fig. S5 Simulation data for 2D parameter sweeps of α-Si nano-posts with height of 800 nm. (a) and (b) Simulated phase shifts and intensity of transmission coefficients of nanostructures for *x*- and *y*-polarization beam with various w_x and w_y. These four graphs constitute the library for the parameters of our PMDP metalens. (c) Simulated polarization conversion rate of each nanostructure for LCP to RCP. (d) Distribution of PCRs for all nanostructures in a PMDP metalens with diameters of 200 μm.

To verify the validity and feasibility of the design, we performed 3D FDTD simulations to evaluate the performance of the PMDP metalens array. For simplicity, we simulated a 2×2 PMDP metalens array that contains 4 LCP lenses and 1 entire RCP lens. We have designed lenses of different geometries: square one and circular one as shown in Fig. S6(a) and Fig. S6(c). For the

square metalens, each one of the nanostructures works as a multiplexing unit for two polarizations, RCP and LCP. While for the circular metalens, only the nanostructures in the overlapping regions of two metalens (pink areas in Fig. S6(c)) are the multiplexing units, and the other nanostructures remain rotated nano-posts to impart phase via PB phase. To save simulation time and memory, we set metalens with the same NA as in experiment but a much smaller size of 10 μm. Figure S6(b) and S6(d) show the results for PMDP metalens arrays focusing at f=12.5 μm for LCP and RCP respectively. Compared to the SNR of circular metalens, the SNR of PMDP metalens with square geometry is much higher, which may be caused by the uniform efficiency for nanostructures at overlapping and non-overlapping regions.

Fig. S6 3D simulation for PMDP metalens. (a) Schematic of square PMDP metalens for LCP (blue squares) and RCP (brown squares). (b) Intensity distributions in focal plane for LCP (left) and RCP (right) of PMDP metalens in (a). (c) Schematic of circular PMDP metalens for LCP (blue circles) and RCP (brown circles). The light pink areas are the overlapping regions that are designed by polarization multiplexing method, while the rest areas only work at expected polarization. (d) Intensity distributions in focal plane for LCP (left) and RCP (right) of PMDP metalens in (c).

Section S6: Images stitching proceeding

Once we obtained the raw images for metalens array, we can have 6×6 sub-images for LCP and 5×5 sub-images for RCP, as shown in Fig. 4(c) and 4(d). In order to get the reconstructed image in Fig. 4(e), we need to stitch the sub-images together. Distortion of sub-images will cause image discontinuity of the stitching image, hence, we first correct the distorted sub-images to improve the image quality.

Digital image processing algorithm for lens distortion：Fortunately, digital image processing methods can effectively correct image distortion through post-processing. For a distorted optical system, the line is no longer a straight one in the image, except for the line through the symmetric center. Therefore, when correcting distortion, the symmetry center should be found first, and then a general geometric distortion correction process should be carried out. General steps of distortion correction are as followed:

(I) Symmetry center estimation: find out the symmetry center of the distorted image, and represent the address of the distorted image as the spatial coordinate relative to symmetric center.

(II) Spatial transformation: the address mapping relation is used to find the corresponding points on the distortion image for each point in the correction image.

(III) Gray interpolation: each point on the correction image is mapped to the distortion image, and then the gray value of this point is obtained by gray interpolation.
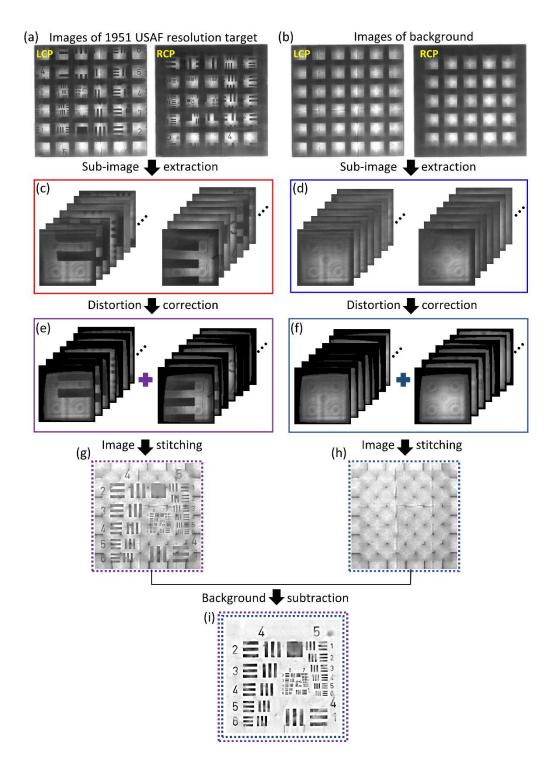
The key of this correction method lies in the estimation of symmetry center and the address mapping between corrected and distorted image. We can use the image of a grid pattern to determine the symmetry center as a benchmark for other complex images taken at the same condition. The address mapping can be obtained with image distortion model (see Ref. [45]).

For each pixel (u,v) in corrected image, we can figure out the corresponding pixel (u',v') in the distorted image with address mapping. Then the pixel value $f(u,v)$ sets as $f'(u',v')$ in distorted image.

u' and v' may be non-integer, which is meaningless in matrix or pixel. In this case, the pixel values at non-integer pixels are calculated with the pixel values at some integer pixels around them, which is called gray interpolation. Here we use cubic interpolation method to get more accurate results.

Method for image stitching of PMDP metalens array：We use a commercial panoramic image stitching software called PTGui to create high quality stitching image. The overlapping between LCP and RCP sub-images ensures the validity for image stitching in PTGui. Drop all the sub-images into PTGui and it will figure out how they overlap. The image stitching process is shown in Fig. S7. Figure S7(a) shows the two raw images of 1951 USAF resolution test chart for LCP and RCP incident light taken from the metalens array on MIID. Then we can get sub-images from Fig. S7(a) as shown in Fig. S7(c). Distortion of sub-images which can result in mismatch during image stitching is non-ignorable. Hence, before image stitching, distortion correction is necessary (Fig. S7(e)). Direct stitching of distortion-corrected sub-images suffers from image discontinuity at stitching seam, as well as the background pattern caused by non-uniform illumination and image sensor response (see Fig. S7(g)).
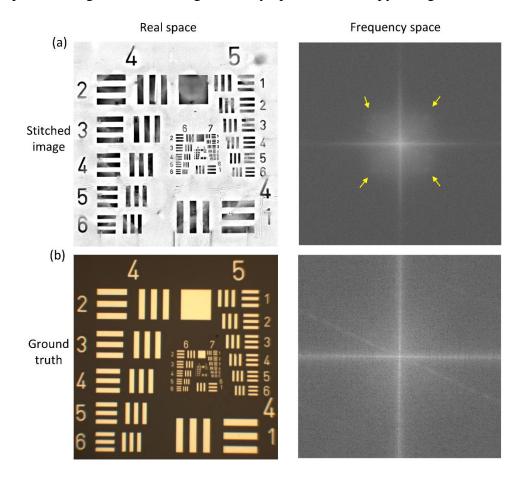
These problems can be eliminated by background subtraction. The raw images of background for LCP and RCP incident light are shown in Fig. S7(b). The stitched image of background (Fig. S7(h)) of corresponding distortion-corrected sub-images (Fig. S7(f)) is formed by the same stitching parameters as image in Fig. S7(g). With background subtraction, the stitched image will be much clearer (see Fig. S7(i)), which is also shown in Fig. 4(e) in the main text.

Fig. S7 Proceeding of image stitching of PMDP metalens array. (a) Raw images of 1951 USAF resolution test chart for LCP and RCP incident light taken from the metalens array on MIID. (b) Raw images of background for LCP and RCP incident light taken from the metalens array on MIID. (c) and (d) Sub-images for raw images in (a) and (b), respectively. (e) and (f) Distortion-corrected sub-images for (c) and (d), respectively. (g) Stitched resolution test chart

image with distortion-corrected sub-images in (e). (h) Stitched background image with distortion-corrected sub-images in (f). (i) Final wide-field image after the background subtraction.

Stitched artifacts of PMDP metalens array：The stitched image has some stitching artifacts such as diagonal stripes due to the uneven brightness at image center and edge caused by vignetting. These artifacts can be clearly seen at the frequency space of the stitched image compared to the frequency space of the ground truth image taken by optical microscopy in Fig. S8.

Fig. S8 Stitched artifacts of PMDP metalens array. (a) Real space and frequency space of the stitched images of 1951 USAF resolution test chart obtained by MIID with PMDP metalens array. The yellow arrows denote the artifacts of the stitched image caused by the uneven brightness at center and edge of sub images. (b) Real space and frequency space of the ground truth obtained by optical microscope with 10× objective.